

ADVANCED MATERIALS INTERFACES

Supporting Information

for *Adv. Mater. Interfaces*, DOI: 10.1002/admi.202200057

Textured and Rigid Capillary Materials for Passive
Energy-Conversion Devices

*Matteo Alberghini, Matteo Morciano, Matteo Giardino,
Francesco Perrucci, Luciano Scaltrito, Davide Janner,
Eliodoro Chiavazzo, Matteo Fasano, and Pietro Asinari**

Textured and rigid capillary materials for passive energy-conversion devices – Supplementary Information –

Matteo Alberghini^{1,2}, Matteo Morciano^{1,2}, Matteo Giardino^{2,3}, Francesco Perrucci^{3,4}, Luciano Scaltrito^{3,4},
Davide Janner^{2,3}, Eliodoro Chiavazzo¹, Matteo Fasano^{1,2}, Pietro Asinari^{1,5,*}

*Corresponding Author, e-mail: pietro.asinari@polito.it

¹Politecnico di Torino, Department of Energy, Corso Duca degli Abruzzi 24, Torino

²Clean Water Center, Corso Duca degli Abruzzi 24, Torino

³Politecnico di Torino, Department of Applied Sciences and Technology, Corso Duca degli Abruzzi 24, Torino

⁴Microla Optoelectronics, Per Via Gozzano 34, Chivasso (Torino)

⁵INRIM, Istituto Nazionale di Ricerca Metrologica, Strada delle Cacce 91, Torino

Supplementary Notes

Supplementary Note S1. Maximum groove width

The capillary suction in micro-porous media is governed by the interplay of the physicochemical properties of the three phases present in the system: the solid porous matrix; a first fluid, generally gaseous (i.e. air); a second fluid, generally a liquid (i.e. water). The balance of forces at the three-phases contact line produce a curvature of the fluid-fluid interface, which generates a pressure difference ΔP across the interface itself according to the Laplace's equation [66]:

$$\Delta P = \gamma_{f,f} \left(\frac{1}{R_1} + \frac{1}{R_2} \right), \quad (\text{S1})$$

where $\gamma_{f,f}$ is the fluid-fluid surface tension, R_1 and R_2 are the main radii of curvature of the fluid-fluid interface, respectively. The shape of the interface, thus the sign of the curvatures, determines which fluid wets the porous matrix, filling its pores. For the sake of simplicity, as the two fluids considered in this work are air and water, the subscript f, f was dropped and the water-air surface tension was simply referred to as γ .

Generally, due to the influence of gravity and the complex shape of the contact line, the radii of curvature are not constant and must be described by second order differential equations. This makes the evaluation of the Laplace's over-pressure, and therefore of the capillary properties of the groove, rather complex. However, gravity might be neglected in straight and small grooves and the water-air interface can be described by a single and constant radius of curvature, while the meniscus can be considered as a cylinder-shaped [36]. The range of validity of these assumptions was investigated considering a tilted hydrophilic plate immersed in water (see Supplementary Fig. S9A). Due to capillarity, the flat water surface bends to form a meniscus which, at the equilibrium, rises up to y_m and extends to x_m , before merging with the unperturbed horizontal surface. The shape of the meniscus in the V-shaped grooves is not affected by gravity if the width of the groove w is small compared to $2x_m$ [67]. Given the tilt angle α and the equilibrium water-plate contact angle θ_e , Eq. S1 was integrated to evaluate x_m .

For a flat plate, the radii of curvature are expressed in Cartesian coordinates as:

$$R_1 = -\frac{(1 + \dot{y}^2)^{3/2}}{\ddot{y}}, \quad (\text{S2})$$

$$R_2 \rightarrow \infty,$$

where $y = y(x)$ is the vertical coordinate and the negative sign is due to the concavity of the water meniscus. Considering vertical capillary rise, Laplace's under-pressure is continuously balanced by gravity, therefore Eqs. S1 and S2 were combined as:

$$\gamma \ddot{y} (1 + \dot{y}^2)^{-3/2} = \rho g y, \quad (\text{S3})$$

where ρ is the water density and g is the gravitational acceleration. The former equation was simplified considering:

$$\frac{d}{dx} \left((1 + \dot{y}^2)^{-1/2} \right) = -\ddot{y} (1 + \dot{y}^2)^{-3/2} \dot{y} \dot{y} = -\frac{1}{l_c^2} y \dot{y}, \quad (\text{S4})$$

where $l_c = \sqrt{\gamma/(\rho g)}$ is the capillary length [66]. Eq. S4 was easily integrated by parts, yielding:

$$(1 + \dot{y}^2)^{-1/2} = \sin \theta = -\frac{1}{2l_c^2} y^2 + c_1, \quad (\text{S5})$$

where θ is the slope of s with respect to the vertical reference. The first equality in Eq. S5 was based on simple geometrical arguments (see the inset in Supplementary Fig. S9A). Considering $\dot{y} = y|_{x \rightarrow \infty} = 0$ as boundary condition, the integration constant was evaluated as $c_1 = 1$. Referring to the symbols of Supplementary Fig. S9A, Eq. S5 was used to derive the maximum height reached by the meniscus y_m :

$$\theta|_{y_m} = \pi/2 - \alpha + \theta_e,$$

$$y_m = l_c \sqrt{2(1 - \cos(\alpha - \theta_e))}. \quad (\text{S6})$$

Eq. S5 was integrated again considering Eq. S6 as boundary condition to obtain the implicit equation of the height of the meniscus y for a given distance x from the wall [66, 68]:

$$x = l_c \left(\operatorname{acosh} \left(\frac{2l_c}{y} \right) - \operatorname{acosh} \left(\frac{2l_c}{y_m} \right) - \sqrt{4 - \frac{y^2}{l_c^2}} + \sqrt{4 - \frac{y_m^2}{l_c^2}} \right). \quad (\text{S7})$$

Eq. S7 predicts $y \rightarrow 0$ for $x \rightarrow \infty$, thus x_m was arbitrarily evaluated as the minimum distance to obtain $y \leq 1 \mu\text{m}$.

The water-plate contact angle θ_e and the plate tilt angle α significantly affect the shape of the water meniscus (see Supplementary Fig. S9B), which has a steeper profile for higher values of α and lower values of θ_e . Supplementary Fig. S9C shows the maximum height reached by the water meniscus (grey-scale map), on the order of centimeters, scaled on the maximum height reached by the meniscus considering similar α and $\theta_e = 0$ (solid red line). This result was used to evaluate the maximum groove width $w = 2x_m$ (see Supplementary Fig. S9D, blue-scale map), which is almost constant for the whole range of α and rapidly decreases to zero as $\alpha \rightarrow \theta_e$. Note that $\theta_e < \alpha$, which represents the necessary condition for the meniscus formation, leading to a net ΔP and, therefore, capillary rise (see Eq. S6). The obtained values of the groove maximum width w are in the order of centimetre, which justifies the assumption of a constant and circular meniscus shape in micro-sized grooves.

Supplementary Note S2. Capillary pressure in micro-sized grooves

Justified by the results presented in section Supplementary Note S1, the effect of gravity on the meniscus shape in sub-millimeter grooves was neglected and, thus, the radius of curvature R was considered constant. As a consequence, Eq. S1 was rewritten as:

$$\Delta P = -\gamma \frac{1}{R} = \gamma \frac{d\theta}{ds} = \gamma \sin(\theta) \frac{d\theta}{dx}, \quad (\text{S8})$$

where s is the planar curve describing the cylindrical water meniscus (see the inset in Supplementary Fig. S10A). Being the radius of curvature R a constant (where the subscript 1 was dropped), Eq. S1 implies constant ΔP . Therefore, Eq. S8 was integrated by separation of variables, leading to:

$$\Delta P = -\frac{2\gamma}{w} \cos(\theta) \Big|_{\pi/2 - \alpha + \theta_e}^{\pi/2}, \quad (\text{S9})$$

where the second boundary condition was formulated considering symmetric grooves, namely $\theta|_{x=w/2} = \pi/2$. Eq. S9 was formulated neglecting the pinning of the water meniscus at the edges of the groove [36]. Being the height of the groove $h_g = w \tan(\alpha)/2$, Eq. S9 was used to obtain the radius of curvature:

$$R = \frac{h_g}{\tan(\alpha) \sin(\alpha - \theta_e)}. \quad (\text{S10})$$

Eq. S10 was written assuming the groove to be entirely filled by water in the y direction, justified by the results presented in section Supplementary Note S1 (see Supplementary Fig. S9C). However, considering a system where gravity is actually negligible (e.g., in horizontal grooves), this assumption can be proved valid by evaluating the derivative of the free energy E given with respect to the meniscus height h , namely dE/dh (see Supplementary Fig. S10B). The free energy per unit length of a V-shaped groove immersed in air and partially wetted by water was evaluated as:

$$\begin{aligned} E &= (\gamma_{s,l} - \gamma_{s,g})A_{s,l} + \gamma A_{l,g} = \\ &= \gamma(A_{l,g} - A_{s,l} \cos(\theta_e)), \end{aligned} \quad (\text{S11})$$

where $\gamma_{s,l}$ and $\gamma_{s,g}$ are the solid-liquid and solid-gas surface tensions, respectively, $A_{s,l}$ and $A_{l,g}$ are the solid-liquid and liquid-gas contact areas, respectively. The second equality was obtained considering the Young-Dupré equation [66, 67], expressing the equilibrium at the three-phases contact line:

$$\gamma_{s,l} + \gamma \cos \theta_e = \gamma_{s,g}. \quad (\text{S12})$$

The contact areas per unit length in the z direction were evaluated as (see Supplementary Fig. S10B):

$$\begin{aligned} A_{s,l} &= \frac{2h}{\sin(\alpha)}, \\ A_{l,g} &= 2R(\alpha - \theta_e) = \frac{2h(\alpha - \theta_e)}{\tan(\alpha) \sin(\alpha - \theta_e)}, \end{aligned} \quad (\text{S13})$$

where, neglecting the effect of gravity, the radius of the water meniscus was expressed according to Eq. S10 for a generic height h . Thus, dE/dh was evaluated as:

$$\frac{dE}{dh} = \gamma \left(\frac{2(\alpha - \theta_e)}{\tan(\alpha) \sin(\alpha - \theta_e)} - \frac{2 \cos(\theta_e)}{\sin(\alpha)} \right). \quad (\text{S14})$$

Being $\theta_e < \alpha$ the condition to have non-zero ΔP , it can be numerically verified that Eq. S14 is negative for any tilt angle in the range $0 < \alpha < 90$, where the extremes of the boundary were willingly omitted.

Supplementary Note S3. Evaporation tests

The water reservoir was made from a polypropylene box (10 cm \times 5 cm, 5 cm high) closed on the upper side by a specifically thermo-formed plastic cover and sealed with silicone to reduce the evaporation losses. A thin slit (12 mm \times 3 mm) was hand-cut on the lid to dip the sample. The reservoir was placed on a high precision balance (Radwag, PS1000 R2), which was used with a sampling frequency of 1 sample/s to assess the evaporation rate. To ensure correct measurement of the evaporation rate, the tested sample and the remaining equipment was placed on an external adjustable support, avoiding any contact with the reservoir or the balance. The external support was composed by a vertical stage, insulating polystyrene foam, a thin copper sheet, three electrical heaters, three 100-ohm PRTs and the tested sample. The polystyrene foam was appropriately shaped and attached to the adjustable vertical stage, forming an insulating support for the sample, the heaters and the PRTs. A thin copper sheet was opportunely cut and connected to the polystyrene foam by double-sided tape. The three electrical heating elements (Franco Corradi, $(32 \pm 1) \Omega$), connected in series, and two 100-ohm PRTs (RS PRO, tolerance class A) were attached to the copper plate facing the insulating foam. The electrical heaters were connected to a power supplier (HQ power, PS 3003) and to a high-precision amperemeter (Agilent, 34401 A). The tested sample was glued on the other side of the copper sheet, facing the environment, by a thin layer of thermal grease (RS PRO, $3.4 \text{ W m}^{-1} \text{ K}^{-1}$) and was then dipped in the reservoir for approximately 5 mm. An extra 100-ohm PRT was used to measure the ambient temperature. The PRTs signals were acquired by a dedicated DAQ device (Pico Instruments, PicoLog PT104).

Supplementary Note S4. Transition to volume averaged parameters

The dynamic imbibition of a single-phase fluid in a saturated, rigid porous matrix under isothermal conditions can be modelled by combining the Darcy's law and the continuity equation [4, 39]:

$$\nabla \cdot \left(-\frac{K}{\phi \mu} (\nabla \langle p \rangle - \rho \mathbf{g}) \right) = 0, \quad (\text{S15})$$

where ϕ and K are respectively the effective porosity and absolute permeability of the porous matrix, $\langle p \rangle$ is the pore-averaged pressure of the fluid. Considering a wicking transient along the grooves axes (in the z

direction for vertical wicking), K can be considered as a constant and Eq. S15 was used to derive a one-dimensional equation for the front position H_t as a function of time. Considering the boundary conditions [4]:

$$\begin{aligned} p \Big|_{z=0} &= p_{atm}, \\ p \Big|_{z=H_t} &= p_{atm} - p_c + \rho g H_t, \end{aligned} \quad (\text{S16})$$

where p_{atm} is the atmospheric pressure, $p_c \sim \Delta P$ is the capillary pressure and the averaging parentheses were dropped for the sake of simplicity. Integration of Eq. S15 in one dimension subject to Eq. S16 leads to:

$$p_c \ln \left| \frac{p_c}{p_c - \rho g H_t} \right| - \rho g H_t = \frac{\rho^2 g^2 K}{\phi \mu} t, \quad (\text{S17})$$

which is indeed equivalent to Eq. S45. By similarity arguments and by defining the absolute porosity ϕ as the ratio between the void and the total volume of material containing the grooves (see Supplementary Fig. S10C), the following definitions hold:

$$\begin{aligned} \phi &= \frac{h_g}{\delta \tan(\alpha)}, \\ K &= \frac{\phi h_g^2 A^*}{8\pi}, \\ p_c &= \frac{\gamma P^*}{h_g A^*}, \end{aligned} \quad (\text{S18})$$

where δ is the center-to-center distance between two adjacent grooves. Eq. S18 coherently links K and p_c to the geometry of the grooves, to the liquid-air surface tension γ and liquid-wall equilibrium contact angle θ_e , and can be used to compare the performances of different, common unstructured capillary materials (e.g. woven or non-woven textiles, foams and hydrogels) to those of the proposed material.

Supplementary Note S5. Evaluation of the wicking parameters of the woven and non-woven textiles

The effective porosity ϕ and capillary pressure p_c of the materials used as reference in Fig. 3C were evaluated experimentally. To measure the effective porosity of the non-woven textiles (green and blue data in Fig. 3C), a large textile sample was entirely submerged in a laboratory-grade graduated cylinder. The volume of the porous matrix V_m was considered as equal to the volume of fluid displaced by the immersion of the sample. An optical microscope (RS PRO) and an image post-processing tool were used to increase the accuracy of the measurement. The total volume of each textile sample V_{tot} was evaluated by measuring its thickness, length and width with a high-resolution caliper. Thus, ϕ was defined as:

$$\phi = 1 - \frac{V_m}{V_{tot}}. \quad (\text{S19})$$

Differently, the porosity of the woven textile (red data in Fig. 3C) was measured by a high-resolution micro-computed tomography scanner (Zeiss Xradia 620 Versa). The complete description of the experimental and numerical methodology used is described in Ref. [4]. The non-woven textile used by Chiavazzo *et al.* [13] (green data) presents $\phi = (0.90 \pm 0.01)$, the one used by Morciano *et al.* [18] (blue data) presents a similar porosity $\phi = (0.87 \pm 0.05)$. Differently, the porosity of the ordered woven fabric developed by Alberghini *et al.* [4] (red data) is significantly lower, namely $\phi = (0.53 \pm 0.05)$.

The capillary pressure of the reference textiles was evaluated by means of capillary rise experiments. At the equilibrium, the capillary pressure is balanced by the gravitational force, namely $p_c = \rho g H_{t,m}$. For this purpose, the setup used for the wicking experiments and described in the Methods section was employed. An optical microscope, a ruler and a image post-processing tool were used to evaluate the height reached by the water front. The steady state was considered reached when the measured $H_{t,m}$ remained constant within a discrepancy of 5%. The resulting values of p_c are shown in Fig. 3D.

Supplementary Note S6. Combining evaporation and the wicking transient: dynamic capillary model

Water tends to evaporate whenever in direct contact with a mixture of gasses non-saturated by its own vapour. Considering a porous medium partially immersed in a wetting fluid and exposed to air, the evaporation rate from the porous surface is driven by the temperature of the two fluids (e.g. water and air) and the content of the fluid vapour in the air. Consequently, evaporation affects the wicking transient and determines the maximum height reached by the water front, which is related to the maximum size of components relying on wicking and evaporation for their operation. Hence, it is essential to model the effect of evaporation on the wicking transient to correctly design passive devices.

The total mass flow rate in the grooves $\dot{M}(z, t)$ (expressed in kg s^{-1}) includes the mass flow rate needed for the advancement of the water front at given time $\dot{M}_{H_t}(t)$, and the mass flow rate needed to balance the fluid evaporating from the wet surface $\dot{M}_e(z, t)$ [40]. Therefore, it holds:

$$\dot{M}(z, t) = \dot{M}_{H_t}(t) + \dot{M}_e(z, t). \quad (\text{S20})$$

$\dot{M}_e(z, t)$ might be caused by one or more specific evaporation rates $\dot{m}_{e,i}^{tot} \geq 0$, which were assumed as constant over a portion of the sample surface. As an example, consider the simplified schematics reported in Fig. S10D-E or Refs. [17, 18]: $\dot{m}_{e,1}^{tot}$ might be zero if the sample was insulated from the surrounding environment, while $\dot{m}_{e,2}^{tot}$ might be governed by membrane transport properties (see Supplementary Note S9) or by specific ambient conditions (e.g., including solar irradiation). Being constants, each specific flux $\dot{m}_{e,i}^{tot}$ assumes the temperature of the evaporating surface to be locally homogeneous and to neglect the progressive build up of vapour above the evaporating surface. The present work accounts for $i = \{1, 2\}$ different fluxes; the generalisation to $i \geq 3$ is beyond the scopes of this work, as the applications considered usually are limited to two zones subject to different conditions.

Referring to the symbols reported in Fig. S10E, the wet grooved aluminum sample is subject to two specific evaporative fluxes:

$$\dot{m}_e(z) = \begin{cases} \dot{m}_{e,1} = 2\dot{m}_{e,1}^{tot}h_g/(\delta \tan(\alpha)) & \text{if } z \leq z_1 \\ \dot{m}_{e,2} = 2\dot{m}_{e,2}^{tot}h_g/(\delta \tan(\alpha)) & \text{if } z > z_1, \end{cases} \quad (\text{S21})$$

where the coefficient $2h_g/(\delta \tan(\alpha))$ was included to consider that, with respect to the sample surface, only the planar projection of the grooves is wet and contributes to evaporation (see Fig. S10C). Considering the height reached by the water front at a given time t , namely H_t , two possible cases must be considered: when $H_t \leq z_1$, the wet portion of the sample is only subject to $\dot{m}_{e,1}$; when $H_t > z_1$, the evaporative flux, thus the mass flow within the grooves, depends on both $\dot{m}_{e,1}$ and $\dot{m}_{e,2}$. For the sake of simplicity, the following equations omit the explicit dependence of the various quantities on the considered time t .

Case 1: $H_t \leq z_1$. The balance of the mass fluxes across an elementary sample volume is (see Fig. S10E):

$$\dot{M} \Big|_z = \dot{M} \Big|_{z+dz} + \dot{m}_{e,1}w dz, \quad (\text{S22})$$

where w is the width of the sample. At the inlet, namely at $z = 0$, the total mass flux includes the flux needed for advancing the water front \dot{M}_{H_t} , and for the flux needed to compensate the evaporation from the whole wet surface $\dot{M}_e = \dot{m}_{e,1}wH_t$ [40]. Integrating Eq. S22 from the inlet to a generic height z , it holds:

$$\int_{\dot{M}_{H_t} + \dot{M}_e}^{\dot{M}_z} d\dot{M} = - \int_0^z \dot{m}_{e,1}w dz, \quad (\text{S23})$$

which can be solved to evaluate the mass flux at a given height $z < H_t$, namely:

$$\dot{M}_z = \dot{M}_{H_t} + \dot{m}_{e,1}wH_t \left(1 - \frac{z}{H_t}\right). \quad (\text{S24})$$

Consequently, \dot{M}_z is linear and has its maximum value at the inlet and decreases as z increases. In general, mass flow rate can be defined in terms of flow velocity v and cross section as $\dot{M} = v\phi h_g w \rho$, where $\phi h_g w$ is

the cross section of the equivalent porous medium and its thickness was assumed to be equal to the height of the grooves h_g (see section Supplementary Note S4 and Fig. S10C). The former relation can be used to define the speed of the evaporating mass flux, namely:

$$v_e \Big|_{H_t \leq z_1} = \frac{\dot{m}_{e,1} H_t}{\phi h_g \rho} \left(1 - \frac{z}{H_t} \right). \quad (\text{S25})$$

Eq. S22 can be reformulated in terms of the fluid velocity:

$$\phi h_g \rho w \left(v_{H_t} \Big|_z + v_e \Big|_z \right) = \phi h_g \rho w \left(v_{H_t} \Big|_{z+dz} + v_e \Big|_{z+dz} \right) + \dot{m}_{e,1} w dz, \quad (\text{S26})$$

which, considering the definition of v_e given in Eq. S25, can be rearranged as:

$$\phi h_g \rho w \frac{v_{H_t} \Big|_{z+dz} - v_{H_t} \Big|_z}{dz} = 0. \quad (\text{S27})$$

Eq. S27 is analogous to the continuity of \dot{M}_{H_t} , namely:

$$\nabla \cdot (v_{H_t}) = 0 \quad (\text{S28})$$

Case 2: $H_t > z_1$. Following the same procedure, substituting Eq. S21 in Eq. S22 and integrating from the inlet to a generic height z , Eq. S24 becomes:

$$\dot{M}_z = \begin{cases} \dot{M}_{H_t} + w \left(\dot{m}_{e,2}(H_t - h_1) + \dot{m}_{e,1} h_1 \left(1 - \frac{z}{z_1} \right) \right) & \text{if } z \leq z_1 \\ \dot{M}_{H_t} + \dot{m}_{e,2} w H_t \left(1 - \frac{z}{H_t} \right) & \text{if } z > z_1. \end{cases} \quad (\text{S29})$$

Recalling the definition of mass flux, Eq. S29 can be used to derive the velocity of the fluid flux needed to balance the effect of evaporation:

$$v_e \Big|_{H_t > z_1} = \begin{cases} \left(\dot{m}_{e,2}(H_t - h_1) + \dot{m}_{e,1} h_1 \left(1 - \frac{z}{z_1} \right) \right) / (\phi h_g \rho) & \text{if } z \leq z_1 \\ \dot{m}_{e,2} H_t \left(1 - \frac{z}{H_t} \right) / (\phi h_g \rho) & \text{if } z > z_1. \end{cases} \quad (\text{S30})$$

Similarly to the previous case, it's easy to show that the substitution of Eq. S30 in S26 leads to Eqs. S27-S28.

Time-discretization. Consider that the water front has reached the height H_t at time t . Therefore, Eqs. S25, S28 and S30 can be used to determine the velocity v_{H_t} of the advancing water front, which can be used to evaluate $H_{t+dt} = H_t + v_{H_t} dt$ at time $t + dt$. The procedure can be iterated to evaluate the curve (H, t) for different grooves shapes and evaporation rates.

For this purpose, Darcy's law was combined with Eq. S28 to evaluate the pressure field of the mass flux \dot{M}_{H_t} at the time t :

$$\nabla^2 p_t = 0, \quad (\text{S31})$$

where the permeability and porosity of the material were assumed as constants. Eq. S31 was solved with a finite differences scheme for each time t by applying proper boundary conditions: in addition to those reported in Eq. S16, an extra pressure drop due to \dot{M}_e was included [40]. Considering the velocity of the evaporating flux v_e , the Darcy's law was used to evaluate the related pressure drop Δp_e for $H_t \leq z_1$:

$$\Delta p_e \Big|_{H_t \leq z_1} = \frac{\mu \phi}{K} \int_0^{H_t} v_e dz = \frac{\mu}{2K h_g \rho} \dot{m}_{e,1} H_t^2, \quad (\text{S32})$$

while Eq. S30 was used for the case $H_t > z_1$:

$$\begin{aligned}\Delta p_e \Big|_{H_t > z_1} &= \frac{\mu \phi}{K} \left(\int_0^{z_1} v_e \Big|_{z \leq z_1} + \int_{z_1}^{H_t} v_e \Big|_{z > z_1} \right) = \\ &= \frac{\mu}{K h_g \rho} \left(z_1 \left(\dot{m}_{e,2}(H_t - z_1) + \frac{1}{2} \dot{m}_{e,1} z_1 \right) + \frac{1}{2} \dot{m}_{e,2}(H_t - z_1)^2 \right).\end{aligned}\quad (\text{S33})$$

Eqs. S32 and S33 were used to reformulate appropriately Eq. S16 to account for evaporation:

$$\begin{aligned}p \Big|_{z=0} &= p_{atm}, \\ p \Big|_{z=H_t} &= \begin{cases} p_{atm} - p_c + \rho g H_t + \Delta p_e \Big|_{H_t \leq z_1} & \text{if } H_t \leq z_1 \\ p_{atm} - p_c + \rho g z_1 + \Delta p_e \Big|_{H_t > z_1} & \text{if } H_t > z_1. \end{cases}\end{aligned}\quad (\text{S34})$$

Eq. S34 was formulated assuming a vertical capillary rise for $z \leq z_1$ and horizontal for $z > z_1$ (see Fig. S10E), coherently with the application investigated in this work. Once the new pressure field at time $t + dt$ was evaluated, the advancing front velocity was computed as:

$$v_{H_t} = \frac{K}{\phi \mu} \frac{p_{H_t} - p_0}{H_t}.\quad (\text{S35})$$

The scheme was iterated until the target simulation time was reached. Being iterative, the procedure requires an initial non-zero height of the water front, as the initial condition $H_t \Big|_{t=0} = 0$ would not be coherent with the model assumptions expressed in section Supplementary Note S8 and would result in an infinite pressure gradient. Thus, being the time-step considered equal to $dt = 0.1$ s, the initial height of the water front $H_t \Big|_{t=dt}$ was evaluated as:

$$H_t \Big|_{t=dt} = \sqrt{\frac{2Kp_c}{\phi \mu} dt},\quad (\text{S36})$$

where the effects of gravity and of evaporation were neglected [39]. The proposed scheme was validated against the analytical relation proposed by Fries *et al.* [40] for vertical capillary rise with a single specific evaporation flux, obtaining excellent agreement.

Supplementary Note S7. Evaluation of the water-aluminium contact angle

Considering the surface of a spherical droplet and referring to the nomenclature reported in Supplementary Fig. S7A, it holds:

$$ds = \frac{dx}{\cos(\phi)} = R d\phi,\quad (\text{S37})$$

where R is the radius of the spherical droplet. Thus, L_d can be evaluated by integrating Eq. S37:

$$L_d = \int_0^{L_d} dx = \int_0^{\theta_e} R \cos(\phi) d\phi = R \sin(\theta_e),\quad (\text{S38})$$

where θ_e is the equilibrium contact angle. The radius of the droplet can be evaluated relying on simple geometrical arguments:

$$R = \frac{L_d^2 + h_d^2}{2h_d}.\quad (\text{S39})$$

Substituting Eq. S39 in Eq. S38, θ_e can be evaluated as:

$$\theta_e = \begin{cases} \arcsin(2L_d h_d / (L_d^2 + h_d^2)) & \text{if } R > h_d \\ \pi - \arcsin(2L_d h_d / (L_d^2 + h_d^2)) & \text{if } R < h_d, \end{cases}\quad (\text{S40})$$

where the cases $R > h_d$ and $R < h_d$ refer to hydrophilic (see Supplementary Fig. S7B) and hydrophobic (see Supplementary Fig. S7C) interactions, respectively.

Supplementary Note S8. Dynamic wicking model

The one-dimensional force balance along the z direction determining capillary rise can be expressed as:

$$F_c = F_\mu + F_g, \quad (\text{S41})$$

where F_c is the capillary force, F_μ is the viscous force and F_g is the gravitational force. To solve Eq. S41, some common simplifying assumptions were considered: as a first approximation, evaporation can be neglected; the gas-liquid surface has a constant shape during imbibition and the height of water meniscus is negligible with respect to the height the water front along the z axis, namely H_t [69]; the flow conditions in the grooves are coherent with a Poiseuille flow, and the viscous losses are determined by the channel cross-section rather than by the shape of the liquid surface [36, 70]; the grooves are completely filled by water and small enough to neglect the effect of gravity on the shape of the meniscus (see section Supplementary Note S2). If these assumptions hold, it can be written:

$$\begin{aligned} F_c &= -\frac{dE}{dz} = h_g \gamma 2 \left(\frac{\cos(\theta_e)}{\sin(\alpha)} - \frac{\alpha - \theta_e}{\tan(\alpha) \sin(\alpha - \theta_e)} \right) = h_g \gamma P^*, \\ F_\mu &= 8\pi\mu z \frac{dz}{dt}, \\ F_g &= \rho g z h_g^2 \left(\frac{1}{\tan^2(\alpha)} \left(\tan(\alpha) + \frac{\cos(\alpha - \theta_e)}{\sin(\alpha - \theta_e)} - \frac{\alpha - \theta_e}{\sin^2(\alpha - \theta_e)} \right) \right) = \rho g z h_g^2 A^*, \end{aligned} \quad (\text{S42})$$

where μ is the dynamic viscosity of the wetting fluid. The free energy was evaluated from Eq. S11, and the cross-sectional area of the channel, namely $h_g^2 A^*$, was evaluated by geometrical arguments from the schematics shown in Supplementary Fig. S10A.

Substituting Eq. S42 in Eq. S41, the position of the water front is described by a first order differential equation:

$$h_g \gamma P^* = 8\pi\mu z \frac{dz}{dt} + h_g^2 A^* \rho g z, \quad (\text{S43})$$

which was re-arranged and integrated by separation of variables:

$$\int_0^t \frac{1}{8\pi\mu} dt = \int_0^{H_t} \frac{z}{A - Bz} dz = \int_0^{H_t} \left(-\frac{A}{B(Bz - A)} - \frac{1}{B} \right) dz, \quad (\text{S44})$$

where $A = h_g P^* \gamma$ and $B = h_g^2 A^* \rho g$. The extremes of integration on the right-hand side were evaluated assuming $z|_{t=0} = 0$ as initial condition, while the front height evaluated at the time t was referred to as $z|_t = H_t$. Solving Eq. S44, the following equation was obtained:

$$\frac{t}{8\pi\mu} = -\frac{A}{B^2} \ln(BH_t - A) - \frac{H_t}{B} + A \ln(-A)/B^2, \quad (\text{S45})$$

which is implicit with respect to H_t . Eq. S45 was made explicit with respect to H_t using the definition of the main branch of the Lambert W function, namely W_0 , which can be used to solve the family of equations $ye^y = x$ in the form $y = W_0(x)$, being $x \geq 0$ and y real numbers. Thus, Eq. S45 was rearranged as:

$$-\exp\left(-1 - \frac{B^2}{8\pi\mu A} t\right) = \frac{BH_t - A}{A} \exp\left(\frac{BH_t - A}{A}\right), \quad (\text{S46})$$

which, given the definition of W_0 , was used to derive the explicit equation of H_t as a function of the wicking time t , namely:

$$H_t = \frac{A}{B} \left(1 + W_0 \left(-\exp\left(-1 - \frac{B^2}{8\pi\mu A} t\right)\right) \right). \quad (\text{S47})$$

Supplementary Note S9. Mass transfer through a micro-porous membrane

The specific flow rate of water vapour through a micro-porous hydrophobic membrane is a complex phenomenon, affected by the vapour chemical potential, the molecular interactions with the other gaseous species (namely, the components of air) and with the porous matrix. This mass transfer of the i -th specie of a mixture through a micro-porous membrane can be expressed by the combined Maxwell-Stefan and dusty-gas models [71]:

$$-\frac{\chi_i}{R_g T} \frac{d\zeta_i}{dy} - \frac{\chi_i K_m \tau_m}{\mu \phi_m D_{i,K}} \frac{dP}{dy} = \sum_{j=1, j \neq i}^n \left(\tau \frac{\chi_j N_i - \chi_i N_j}{c_t D_{ij} \phi_m} \right) + \frac{N_i \tau}{c_t \phi_m D_{i,K}}, \quad (\text{S48})$$

where χ_i and ζ_i are the molar fraction and chemical potential of species i , R_g is the ideal gas constant, T is the average temperature of the system, c_t is the total molar concentration, N_i is the molar flux of species i , n is the total number of components in the mixture, P is the bulk fluid pressure. K_m , τ_m and ϕ_m are respectively the absolute permeability, tortuosity and effective porosity of the membrane, which are considered as constant. D_{ij} is the diffusion coefficient of species i in species j and $D_{i,K}$ is the Knudsen diffusion coefficient. Eq. S48 was written considering one-dimensional mass transfer, justified by the large aspect ratio of the membrane. Eq. S48 was simplified and solved analytically by relying on some common approximations: the non-condensable components of air were considered as a single gas, reducing the system to only two components, namely water vapour and air; both components were considered as ideal gasses [13, 17, 18], thus allowing to rewrite the chemical potential as: $\zeta_i = \zeta_{i,0} + R_g T \ln(\chi_i)$, where $\zeta_{i,0}$ is the chemical potential of pure species i ; the temperature and pressure gradients are negligible in the evaluation of the chemical potential; the contribute of the viscous flow can be neglected [72]; the air in the membrane can be considered as still, thus its molar flux was set to zero [13, 17, 18, 72]. Thus, Eq. S48 was rewritten for the water vapour as:

$$-\frac{d\chi_w}{dy} = \frac{\tau_m N_w}{\phi_m c_t D_{wa}} \left(1 - \chi_w + \frac{D_{wa}}{D_{w,K}} \right), \quad (\text{S49})$$

where the subscripts w and a refer to water vapour and air, respectively. Eq. S49 was integrated by separation of variables across the thickness of the membrane d_m :

$$\int_{\chi_{w,e}}^{\chi_{w,c}} -\frac{d\chi_w}{1 + \beta_D - \chi_w} = \int_0^{d_m} \frac{\tau_m N_w}{\phi_m c_t D_{wa}} dy, \quad (\text{S50})$$

where $\beta_D = D_{wa}/D_{w,K}$. In Eq. S50, the molar fraction at the evaporator and at the condenser were respectively evaluated by their partial pressure, namely:

$$\begin{aligned} \chi_w |_{y=0} &= \chi_{w,e} = p_w^e(T_e) a_e / P \\ \chi_w |_{y=d_m} &= \chi_{w,c} = p_w^e(T_c) a_c / P, \end{aligned} \quad (\text{S51})$$

where $p_w^e(T_e)$ and $p_w^e(T_c)$ are respectively the temperature-dependent effective vapour pressure at the evaporator and at the condenser, a_e and a_c are the activity coefficients of the solutions at each end of the membrane [17], which account for the presence of salt on the evaporator side.

Considering a flat liquid surface in equilibrium with the surrounding environment, the vapour pressure p_w , expressed in Pa, can be evaluated by the Antoine's equation:

$$p_w = \frac{101.325}{760} 10^{A-B/(C-T)}, \quad (\text{S52})$$

where $A = 8.07$, $B = 1730.63$ and $C = 233.42$ are component-specific constants and T is the reference temperature, expressed in degrees Celsius. To consider the effect of the meniscus curvature at the water-air interface, the vapour pressure was corrected according to the Kelvin's equation to the effective value p_w^e :

$$p_w^e = p_w \exp \left(\frac{p_w^e - p_w - \gamma/R}{\rho R_g T} \right), \quad (\text{S53})$$

where p_w is the equilibrium vapour pressure evaluated by Eq. S52, R is the meniscus curvature evaluated by Eq. S10 (see Supplementary Note S2), γ is the liquid-air surface tension and T is the reference temperature, expressed in Kelvin. Clearly, if the liquid-air interface is flat (namely $R \rightarrow \infty$) Eq. S53 leads to $p_w^e \rightarrow p_w$. Eq. S53 is implicit, and was iteratively solved to evaluate the effective vapor pressure p_w^e above the evaporating meniscus and was used in Eq. S51 to evaluate the extremes of integration of Eq. S50. The activity coefficients of water-salt solutions were estimated by the Raoult law for ideal mixtures, which is valid in the limit of low concentrations:

$$a \approx \frac{1}{1 + mM_w N_i}, \quad (\text{S54})$$

where m is the molality of the solution, M_w is the molar mass of water and N_i is the number of ions composing the salt, assuming complete dissociation. Clearly, $a = 1$ for distilled water, while the activity coefficient decreases at higher solute concentrations. Thus, the specific mass flow rate of water vapour J_w was evaluated as:

$$J_w = N_w M_w = \frac{\phi_m c_t D_{wa} M_w}{\tau_m d_m} \ln \left(\frac{1 - \frac{p_w^e(T_e) a_e}{P(1+\beta_D)}}{1 - \frac{p_w^e(T_e) a_e}{P(1+\beta_D)}} \right), \quad (\text{S55})$$

where D_{wa} and c_t were assumed as constant in the interval of integration.

A possible configuration for membrane distillation devices include a porous spacer in series to the microporous hydrophobic membrane [17, 18]. Considering a plastic support with thickness d_s , porosity ϕ_s and unitary tortuosity (i.e., straight cylindrical pores), the molar fraction of the water vapour at the evaporator side, at the interface between the membrane and the support, and at the condenser side were respectively evaluated as:

$$\begin{aligned} \chi_w |_{y=0} &= \chi_{w,e} = p_w^e(T_e) a_e / P \\ \chi_w |_{y=d_m} &= \chi_{w,s} = p_w(T_s) a_s / P \\ \chi_w |_{y=d_s+d_m} &= \chi_{w,c} = p_w^e(T_c) a_c / P, \end{aligned} \quad (\text{S56})$$

where the activity coefficient at both ends of the spacer are unitary, as, thanks to the hydrophobic membrane, for $y > d_m$ the water vapour only faces distilled water. Thus, the specific mass flux of water vapour J_w flowing through the spacer was obtained by integrating Eq. S49 with the boundary conditions expressed in Eq. S56, obtaining:

$$J_w = \frac{\phi_s c_t D_{wa} M_w}{d_s} \ln \left(\frac{1 - \frac{p_w^e(T_c)}{P}}{1 - \frac{p_w^e(T_s)}{P}} \right), \quad (\text{S57})$$

where the large and straight pores of the spacer allowed to assume $\beta_D \approx 0$ and $\tau_s \approx 1$, thus neglecting Knudsen diffusion in the spacer.

If $\chi_w \ll 1$, Eqs. S57 and S55 can be linearised by a first-order Taylor series, leading to:

$$\begin{aligned} J_w \Big|_{y=0}^{y=d_m} &= \frac{\phi_m D_{wa} M_w}{\tau_m d_m R_g \bar{T}_m} \frac{1}{(1 + \beta_D)} (p_w(T_s) - a_e p_w^e(T_e)) = C_1 \Delta P_m \\ J_w \Big|_{y=d_m}^{y=d_m+d_s} &= \frac{\phi_s D_{wa} M_w}{d_s R_g \bar{T}_s} (p_w^e(T_c) - p_w(T_s)) = C_2 \Delta P_s, \end{aligned} \quad (\text{S58})$$

where the activity coefficients at $y = d_m$ and $y = d_m + d_s$ were assumed as unitary, ΔP_m and ΔP_s are respectively the pressure drops across the membrane and the spacer, \bar{T}_m and \bar{T}_s are respectively the average temperature within the membrane and the spacer. Eq. S58 allows to interpret the fluxes of water vapour with an electrical analogy, thus as driven by a pressure difference ΔP_i through a porous layer with resistance $B_i = 1/C_i$. Therefore, relying on continuity:

$$\begin{aligned} J_w \Big|_{y=0}^{y=d_m+d_s} &= B (p_w^e(T_c) - a_e p_w^e(T_e)) = \\ J_w \Big|_{y=d_m}^{y=d_m+d_s} &= C_2 (p_w^e(T_c) - p_w(T_s)), \end{aligned} \quad (\text{S59})$$

where $B = 1/C_1 + 1/C_2$ is the total resistance opposed to the mass transport by the membrane and the spacer, expressed as a series of resistances, namely:

$$\frac{1}{B} = \frac{d_m \tau_m R_g \bar{T}_m \bar{p}_{a,m}}{\phi_m D_{wa} M_w P} + \frac{d_m \tau_m R_g \bar{T}_m}{\phi_m D_{w,K} M_w} + \frac{d_a R_g \bar{T}_a \bar{p}_{a,s}}{\phi_a D_{wa} M_w P}, \quad (\text{S60})$$

where the first and third term at the second member were corrected by the factor $\bar{p}_{a,m/s}/P$, being $\bar{p}_{a,m/s}$ the averaged partial pressure of air in the membrane or in the spacer, which has been used in several studies to obtain a better approximation of experimental results [13].

Finally, Eqs. S59 and S60, obtained from the linearisation of the specific mass fluxes performed in Eq. S58, can be used in the non-linearised equation of the specific water vapour flux through the membrane to express $p_w(T_s)$, obtaining a less crude approximation of J_w , namely:

$$J_w = \frac{\phi_m D_{wa} M_w P}{\tau_m d_m R_g \bar{T}_m} \ln \left(\frac{1 - (p_w^e(T_c) - \frac{B}{C_2} (p_w^e(T_c) - a_e p_w^e(T_e)))/P(1 + \beta_D)}{1 - a_e p_w^e(T_e)/(P(1 + \beta_D))} \right). \quad (\text{S61})$$

The parameter PD_{wa} in Eqs. S60 and S61 was evaluated from the empirical relation $PD_{wa} = 1.19 \times 10^{-4} T^{1.75}$ (expressed in $\text{Pa m}^2 \text{ s}^{-1}$) [73], the Knudsen diffusion coefficient for water vapour at a reference temperature is defined as [71]:

$$D_{w,K} = \frac{\phi_{me} d_p}{3\tau_{me}} \sqrt{\frac{8R_g \bar{T}}{\pi M_w}}, \quad (\text{S62})$$

where d_p is the average size of pores diameter and τ_{me} is the membrane tortuosity, which is correlated to the membrane porosity through [74]:

$$\tau_m = \frac{(2 - \phi_m)^2}{\phi_m}. \quad (\text{S63})$$

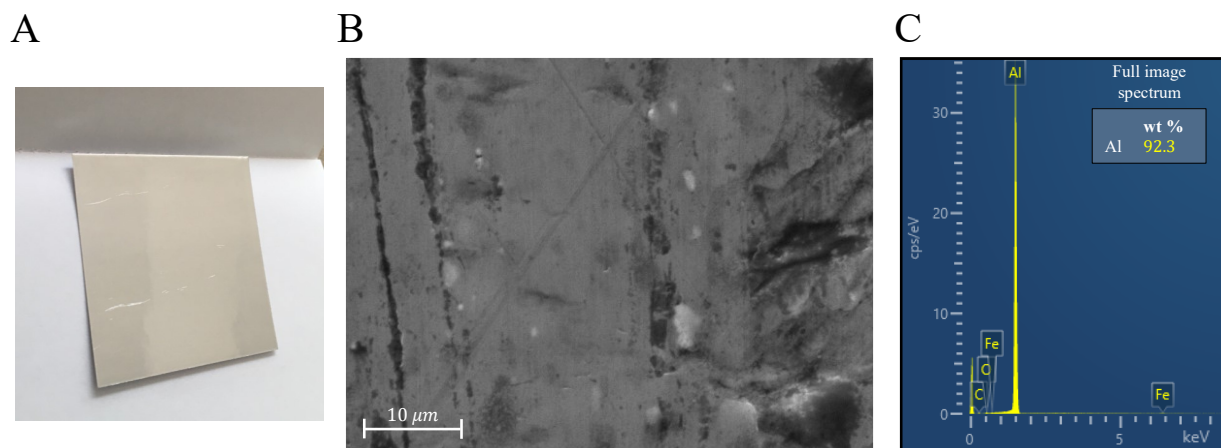
References

- [1] N. A. Dudukovic, E. J. Fong, H. B. Gameda, J. R. DeOtte, M. R. Cerón, B. D. Moran, J. T. Davis, S. E. Baker, E. B. Duoss, Cellular fluidics, *Nature* 595 (7865) (2021) 58–65.
- [2] P. Liu, G.-F. Chen, Porous materials: processing and applications, Elsevier, 2014.
- [3] B. Buonomo, A. di Pasqua, O. Manca, S. Nardini, Evaluation of thermal and fluid dynamic performance parameters in aluminum foam compact heat exchangers, *Applied Thermal Engineering* 176 (2020) 115456.
- [4] M. Alberghini, S. Hong, L. M. Lozano, V. Korolovych, Y. Huang, F. Signorato, S. H. Zandavi, C. Fucetola, I. Uluturk, M. Y. Tolstorukov, et al., Sustainable polyethylene fabrics with engineered moisture transport for passive cooling, *Nature Sustainability* (2021) 1–10.
- [5] J. Lee, J. Kim, T. Hyeon, Recent progress in the synthesis of porous carbon materials, *Advanced materials* 18 (16) (2006) 2073–2094.
- [6] S. C. Singh, M. ElKabbash, Z. Li, X. Li, B. Regmi, M. Madsen, S. A. Jalil, Z. Zhan, J. Zhang, C. Guo, Solar-trackable super-wicking black metal panel for photothermal water sanitation, *Nature Sustainability* 3 (11) (2020) 938–946.
- [7] S. J. Hollister, Porous scaffold design for tissue engineering, *Nature materials* 4 (7) (2005) 518–524.
- [8] M. E. Davis, Ordered porous materials for emerging applications, *Nature* 417 (6891) (2002) 813–821.
- [9] M. Fasano, L. Ventola, F. Calignano, D. Manfredi, E. P. Ambrosio, E. Chiavazzo, P. Asinari, Passive heat transfer enhancement by 3d printed pitot tube based heat sink, *International Communications in Heat and Mass Transfer* 74 (2016) 36–39.
- [10] L. Ventola, M. Fasano, R. Cappabianca, L. Bergamasco, F. Clerici, L. Scaltrito, E. Chiavazzo, P. Asinari, Convective heat transfer enhancement through laser-etched heat sinks: Elliptic scale-roughened and cones patterns, *Energies* 13 (6) (2020) 1360.
- [11] S. V. Boriskina, A. Raza, T. Zhang, P. Wang, L. Zhou, J. Zhu, Nanomaterials for the water-energy nexus, *MRS Bulletin* 44 (1) (2019) 59–66.
- [12] M. Morciano, M. Fasano, U. Salomov, L. Ventola, E. Chiavazzo, P. Asinari, Efficient steam generation by inexpensive narrow gap evaporation device for solar applications, *Scientific reports* 7 (1) (2017) 1–9.
- [13] E. Chiavazzo, M. Morciano, F. Viglino, M. Fasano, P. Asinari, Passive solar high-yield seawater desalination by modular and low-cost distillation, *Nature sustainability* 1 (12) (2018) 763–772.
- [14] S.-L. Wu, H. Chen, H.-L. Wang, X. Chen, H.-C. Yang, S. B. Darling, Solar-driven evaporators for water treatment: challenges and opportunities, *Environmental Science: Water Research & Technology* 7 (1) (2021) 24–39.

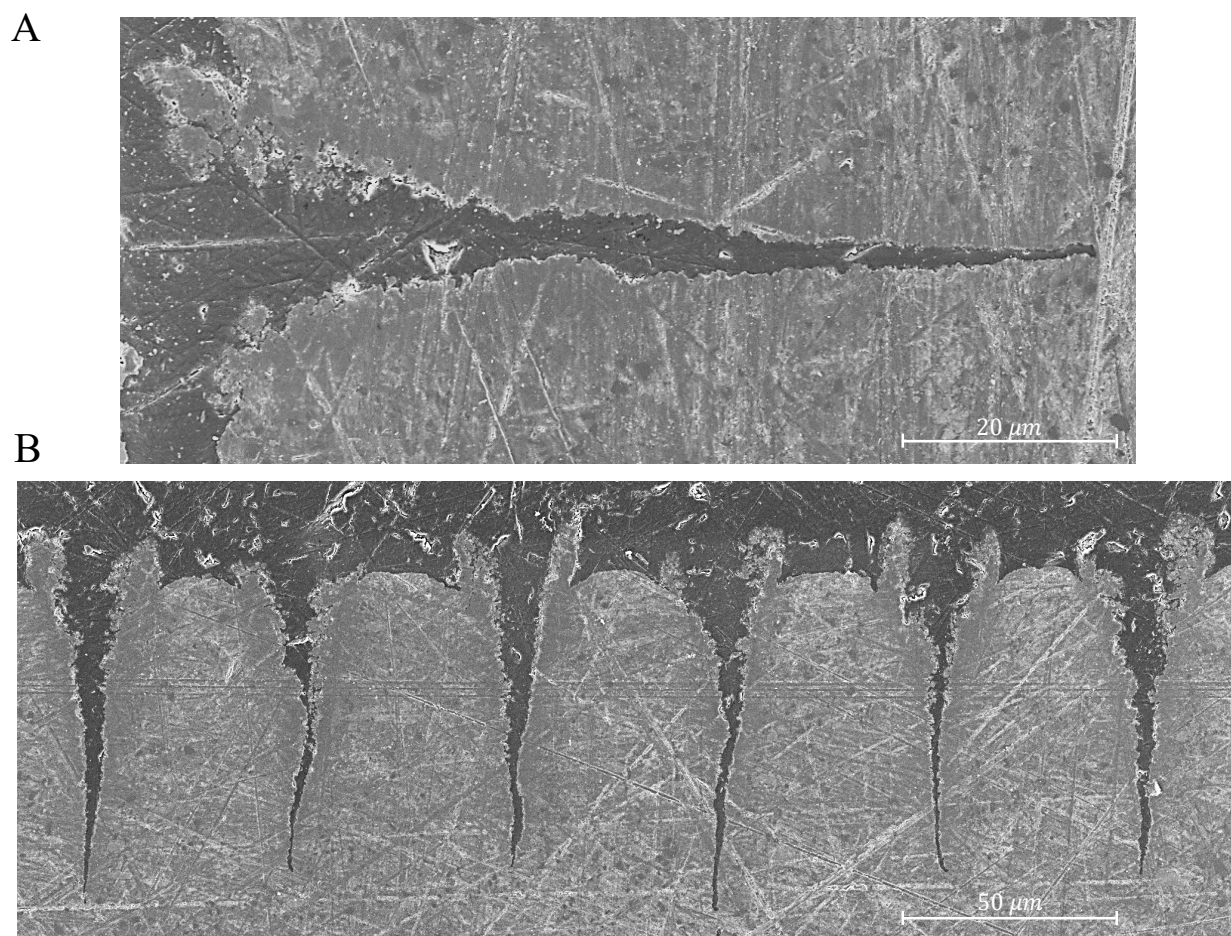
- [15] C. Zhang, Y. Shi, L. Shi, H. Li, R. Li, S. Hong, S. Zhuo, T. Zhang, P. Wang, Designing a next generation solar crystallizer for real seawater brine treatment with zero liquid discharge, *Nature communications* 12 (1) (2021) 1–10.
- [16] L. Zhao, B. Bhatia, L. Zhang, E. Strobach, A. Leroy, M. K. Yadav, S. Yang, T. A. Cooper, L. A. Weinstein, A. Modi, et al., A passive high-temperature high-pressure solar steam generator for medical sterilization, *Joule* 4 (12) (2020) 2733–2745.
- [17] M. Alberghini, M. Morciano, M. Fasano, F. Bertiglia, V. Fericola, P. Asinari, E. Chiavazzo, Multistage and passive cooling process driven by salinity difference, *Science advances* 6 (11) (2020) eaax5015.
- [18] M. Morciano, M. Fasano, S. V. Boriskina, E. Chiavazzo, P. Asinari, Solar passive distiller with high productivity and marangoni effect-driven salt rejection, *Energy & Environmental Science* 13 (10) (2020) 3646–3655.
- [19] C. Chen, Y. Kuang, L. Hu, Challenges and opportunities for solar evaporation, *Joule* 3 (3) (2019) 683–718.
- [20] S. H. Kim, G. C. Lee, J. Y. Kang, K. Moriyama, M. H. Kim, H. S. Park, Boiling heat transfer and critical heat flux evaluation of the pool boiling on micro structured surface, *International Journal of Heat and Mass Transfer* 91 (2015) 1140–1147.
- [21] A. Olanrewaju, M. Beaugrand, M. Yafia, D. Juncker, Capillary microfluidics in microchannels: from microfluidic networks to capillary circuits, *Lab on a Chip* 18 (16) (2018) 2323–2347.
- [22] L. Ventola, L. Scaltrito, S. Ferrero, G. Maccioni, E. Chiavazzo, P. Asinari, Micro-structured rough surfaces by laser etching for heat transfer enhancement on flush mounted heat sinks, in: *Journal of Physics: Conference Series*, IOP Publishing, 2014, p. 012017.
- [23] J. Drelich, E. Chibowski, D. D. Meng, K. Terpilowski, Hydrophilic and superhydrophilic surfaces and materials, *Soft Matter* 7 (21) (2011) 9804–9828.
- [24] S. Divin-Mariotti, P. Amieux, A. Pascale-Hamri, V. Auger, G. Kermouche, F. Valiorgue, S. Valette, Effects of micro-knurling and femtosecond laser micro texturing on aluminum long-term surface wettability, *Applied Surface Science* 479 (2019) 344–350.
- [25] A.-M. Kietzig, M. Negar Mirvakili, S. Kamal, P. Englezos, S. G. Hatzikiriakos, Laser-patterned super-hydrophobic pure metallic substrates: Cassie to wenzel wetting transitions, *Journal of Adhesion Science and Technology* 25 (20) (2011) 2789–2809.
- [26] P. Bizi-Bandoki, S. Valette, E. Audouard, S. Benayoun, Time dependency of the hydrophilicity and hydrophobicity of metallic alloys subjected to femtosecond laser irradiations, *Applied Surface Science* 273 (2013) 399–407.
- [27] G. Antonetto, M. Morciano, M. Alberghini, G. Malgaroli, A. Ciocia, L. Bergamasco, F. Spertino, M. Fasano, Synergistic freshwater and electricity production using passive membrane distillation and waste heat recovered from camouflaged photovoltaic modules, *Journal of Cleaner Production* 318 (2021) 128464.
- [28] M. Morciano, M. Fasano, L. Bergamasco, A. Albiero, M. L. Curzio, P. Asinari, E. Chiavazzo, Sustainable freshwater production using passive membrane distillation and waste heat recovery from portable generator sets, *Applied Energy* 258 (2020) 114086.
- [29] D. Vasconcelos, J. Carvalho, M. Mantel, W. Vasconcelos, Corrosion resistance of stainless steel coated with sol-gel silica, *Journal of non-crystalline solids* 273 (1-3) (2000) 135–139.
- [30] K.-H. Choi, J.-A. Jeong, J.-W. Kang, D.-G. Kim, J. K. Kim, S.-I. Na, D.-Y. Kim, S.-S. Kim, H.-K. Kim, Characteristics of flexible indium tin oxide electrode grown by continuous roll-to-roll sputtering process for flexible organic solar cells, *Solar Energy Materials and Solar Cells* 93 (8) (2009) 1248–1255.
- [31] L. Bonandini, N. Barbero, K. Costabello, C. Pavan, F. Parisi, G. Viscardi, Roll-to-roll atmospheric plasma treatment: A green and efficient process to improve the hydrophilicity of a pet surface, *ChemSusChem: Chemistry & Sustainability Energy & Materials* 3 (5) (2010) 591–596.
- [32] P. Tao, G. Ni, C. Song, W. Shang, J. Wu, J. Zhu, G. Chen, T. Deng, Solar-driven interfacial evaporation, *Nature energy* 3 (12) (2018) 1031–1041.
- [33] Z. Wang, T. Horseman, A. P. Straub, N. Y. Yip, D. Li, M. Elimelech, S. Lin, Pathways and challenges for efficient solar-thermal desalination, *Science advances* 5 (7) (2019) eaax0763.
- [34] L. Zhang, Z. Xu, L. Zhao, B. Bhatia, Y. Zhong, S. Gong, E. N. Wang, Passive, high-efficiency thermally-localized solar desalination, *Energy & Environmental Science* 14 (4) (2021) 1771–1793.
- [35] Y. Zhang, T. Xiong, D. K. Nandakumar, S. C. Tan, Structure architecting for salt-rejecting solar interfacial desalination to achieve high-performance evaporation with in situ energy generation, *Advanced Science* 7 (9) (2020) 1903478.
- [36] R. Rye, J. Mann, F. Yost, The flow of liquids in surface grooves, *Langmuir* 12 (2) (1996) 555–565.
- [37] D. Yang, M. Krasowska, C. Priest, M. N. Popescu, J. Ralston, Dynamics of capillary-driven flow in open microchannels, *The Journal of Physical Chemistry C* 115 (38) (2011) 18761–18769.
- [38] E. W. Washburn, The dynamics of capillary flow, *Physical review* 17 (3) (1921) 273.
- [39] R. Masoodi, K. M. Pillai, *Wicking in porous materials: traditional and modern modeling approaches*, CRC Press, 2012.
- [40] N. Fries, K. Odic, M. Conrath, M. Dreyer, The effect of evaporation on the wicking of liquids into a metallic weave, *Journal of colloid and interface science* 321 (1) (2008) 118–129.
- [41] T. Hata, Y. Kitazaki, T. Saito, Estimation of the surface energy of polymer solids, *The Journal of Adhesion* 21 (3-4) (1987) 177–194.
- [42] D. Quéré, Non-sticking drops, *Reports on Progress in Physics* 68 (11) (2005) 2495.
- [43] Y. Ito, Y. Tanabe, J. Han, T. Fujita, K. Tanigaki, M. Chen, Multifunctional porous graphene for high-efficiency steam generation by heat localization, *Advanced Materials* 27 (29) (2015) 4302–4307.
- [44] L. Shi, Y. Wang, L. Zhang, P. Wang, Rational design of a bi-layered reduced graphene oxide film on polystyrene foam for solar-driven interfacial water evaporation, *Journal of Materials Chemistry A* 5 (31) (2017) 16212–16219.
- [45] P. Zhang, J. Li, L. Lv, Y. Zhao, L. Qu, Vertically aligned graphene sheets membrane for highly efficient solar thermal generation of clean water, *ACS nano* 11 (5) (2017) 5087–5093.

- [46] L. Cui, P. Zhang, Y. Xiao, Y. Liang, H. Liang, Z. Cheng, L. Qu, High rate production of clean water based on the combined photo-electro-thermal effect of graphene architecture, *Advanced Materials* 30 (22) (2018) 1706805.
- [47] N. Xu, X. Hu, W. Xu, X. Li, L. Zhou, S. Zhu, J. Zhu, Mushrooms as efficient solar steam-generation devices, *Advanced Materials* 29 (28) (2017) 1606762.
- [48] M. Zhu, Y. Li, G. Chen, F. Jiang, Z. Yang, X. Luo, Y. Wang, S. D. Lacey, J. Dai, C. Wang, et al., Tree-inspired design for high-efficiency water extraction, *Advanced Materials* 29 (44) (2017) 1704107.
- [49] M. Higgins, A. S. Rahmaan, R. R. Devarapalli, M. V. Shelke, N. Jha, Carbon fabric based solar steam generation for waste water treatment, *Solar Energy* 159 (2018) 800–810.
- [50] Y. Wang, L. Zhang, P. Wang, Self-floating carbon nanotube membrane on macroporous silica substrate for highly efficient solar-driven interfacial water evaporation, *ACS Sustainable Chemistry & Engineering* 4 (3) (2016) 1223–1230.
- [51] C. Chen, Y. Li, J. Song, Z. Yang, Y. Kuang, E. Hitz, C. Jia, A. Gong, F. Jiang, J. Zhu, et al., Highly flexible and efficient solar steam generation device, *Advanced Materials* 29 (30) (2017) 1701756.
- [52] H. Ghasemi, G. Ni, A. M. Marconnet, J. Loomis, S. Yerci, N. Miljkovic, G. Chen, Solar steam generation by heat localization, *Nature communications* 5 (1) (2014) 1–7.
- [53] X. Huang, Y.-H. Yu, O. L. de Llergo, S. M. Marquez, Z. Cheng, Facile polypyrrole thin film coating on polypropylene membrane for efficient solar-driven interfacial water evaporation, *RSC advances* 7 (16) (2017) 9495–9499.
- [54] Q. Chen, Z. Pei, Y. Xu, Z. Li, Y. Yang, Y. Wei, Y. Ji, A durable monolithic polymer foam for efficient solar steam generation, *Chemical science* 9 (3) (2018) 623–628.
- [55] F. Zhao, X. Zhou, Y. Shi, X. Qian, M. Alexander, X. Zhao, S. Mendez, R. Yang, L. Qu, G. Yu, Highly efficient solar vapour generation via hierarchically nanostructured gels, *Nature nanotechnology* 13 (6) (2018) 489–495.
- [56] J. Wang, Y. Li, L. Deng, N. Wei, Y. Weng, S. Dong, D. Qi, J. Qiu, X. Chen, T. Wu, High-performance photothermal conversion of narrow-bandgap Ti_2O_3 nanoparticles, *Advanced Materials* 29 (3) (2017) 1603730.
- [57] X. Wang, Y. He, X. Liu, L. Shi, J. Zhu, Investigation of photothermal heating enabled by plasmonic nanofluids for direct solar steam generation, *Solar Energy* 157 (2017) 35–46.
- [58] J. Zhao, Y. Yang, C. Yang, Y. Tian, Y. Han, J. Liu, X. Yin, W. Que, A hydrophobic surface enabled salt-blocking 2d $\text{Ti}_3\text{C}_2\text{MX}_2$ membrane for efficient and stable solar desalination, *Journal of Materials Chemistry A* 6 (33) (2018) 16196–16204.
- [59] S. Hong, Y. Shi, R. Li, C. Zhang, Y. Jin, P. Wang, Nature-inspired, 3d origami solar steam generator toward near full utilization of solar energy, *ACS applied materials & interfaces* 10 (34) (2018) 28517–28524.
- [60] X. Li, J. Li, J. Lu, N. Xu, C. Chen, X. Min, B. Zhu, H. Li, L. Zhou, S. Zhu, et al., Enhancement of interfacial solar vapor generation by environmental energy, *Joule* 2 (7) (2018) 1331–1338.
- [61] Y. Shi, R. Li, Y. Jin, S. Zhuo, L. Shi, J. Chang, S. Hong, K.-C. Ng, P. Wang, A 3d photothermal structure toward improved energy efficiency in solar steam generation, *Joule* 2 (6) (2018) 1171–1186.
- [62] G. Xue, Q. Chen, S. Lin, J. Duan, P. Yang, K. Liu, J. Li, J. Zhou, Highly efficient water harvesting with optimized solar thermal membrane distillation device, *Global Challenges* 2 (5-6) (2018) 1800001.
- [63] W. Wang, Y. Shi, C. Zhang, S. Hong, L. Shi, J. Chang, R. Li, Y. Jin, C. Ong, S. Zhuo, et al., Simultaneous production of fresh water and electricity via multistage solar photovoltaic membrane distillation, *Nature communications* 10 (1) (2019) 1–9.
- [64] Z. Xu, L. Zhang, L. Zhao, B. Li, B. Bhatia, C. Wang, K. L. Wilke, Y. Song, O. Labban, J. H. Lienhard, et al., Ultrahigh-efficiency desalination via a thermally-localized multistage solar still, *Energy & Environmental Science* 13 (3) (2020) 830–839.
- [65] W. Wang, Y. Shi, C. Zhang, R. Li, M. Wu, S. Zhuo, S. Aleid, P. Wang, Solar seawater distillation by flexible and fully passive multistage membrane distillation, *Nano Letters* (2021).
- [66] P.-G. De Gennes, F. Brochard-Wyart, D. Quéré, *Capillarity and wetting phenomena: drops, bubbles, pearls, waves*, Springer Science & Business Media, 2013.
- [67] A. Faghri, Y. Zhang, *Transport phenomena in multiphase systems*, Elsevier, 2006.
- [68] G. Soligno, M. Dijkstra, R. van Roij, The equilibrium shape of fluid-fluid interfaces: Derivation and a new numerical method for young’s and young-laplace equations, *The Journal of chemical physics* 141 (24) (2014) 244702.
- [69] H. Princen, Capillary phenomena in assemblies of parallel cylinders: I. capillary rise between two cylinders, *Journal of Colloid and Interface Science* 30 (1) (1969) 69–75.
- [70] D. Deng, Y. Tang, J. Zeng, S. Yang, H. Shao, Characterization of capillary rise dynamics in parallel micro v-grooves, *International Journal of Heat and Mass Transfer* 77 (2014) 311–320.
- [71] R. Krishna, J. Wesselingh, The maxwell-stefan approach to mass transfer, *Chemical engineering science* 52 (6) (1997) 861–911.
- [72] A. Deshmukh, M. Elimelech, Understanding the impact of membrane properties and transport phenomena on the energetic performance of membrane distillation desalination, *Journal of Membrane Science* 539 (2017) 458–474.
- [73] Y. Yun, R. Ma, W. Zhang, A. Fane, J. Li, Direct contact membrane distillation mechanism for high concentration nacl solutions, *Desalination* 188 (1-3) (2006) 251–262.
- [74] J. Mackie, P. Meares, The diffusion of electrolytes in a cation-exchange resin membrane i. theoretical, *Proceedings of the Royal Society of London. Series A. Mathematical and Physical Sciences* 232 (1191) (1955) 498–509.

Supplementary figures

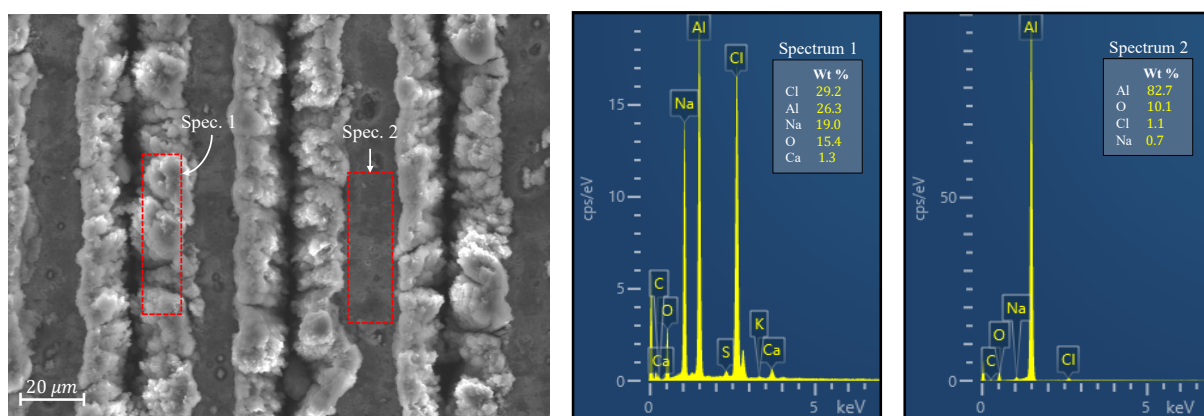


Supplementary Figure S1: **Characterization of the as-received aluminium sheet.** (A) Photograph and (B) SEM image of the high-purity aluminium sheet (5 cm × 5 cm). (C) EDS spectroscopy of the as-received material. The tests show a high presence of aluminum on the surface. However, the aluminum content on the sample is lower than the declared 99% and might be responsible of the high measured value of the contact angle with water. Elements not shown in the legend were present in a non-significant amount.

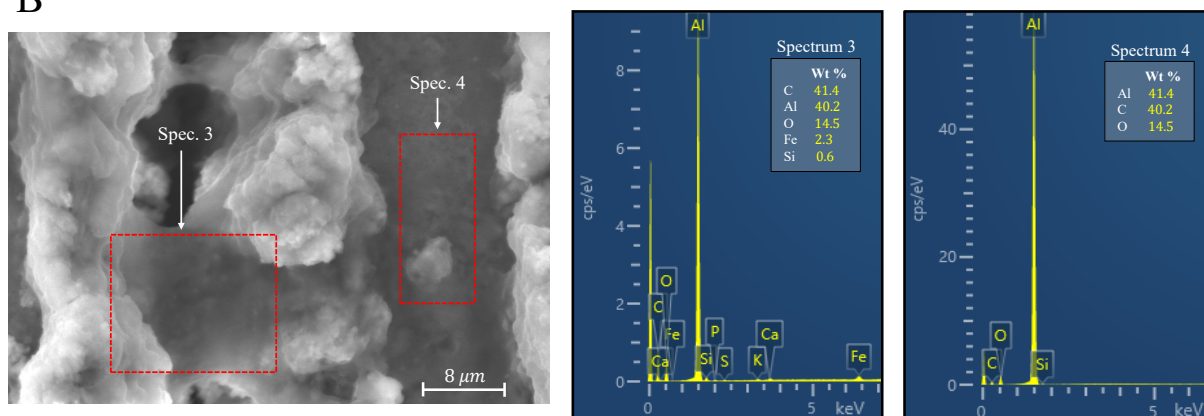


Supplementary Figure S2: **Cross-sectional images of the grooved aluminum sample.** (A) Close-up and (B) full-scale SEM images of the laser-etched material. See the Methods section for a description of the procedure used to obtain the images.

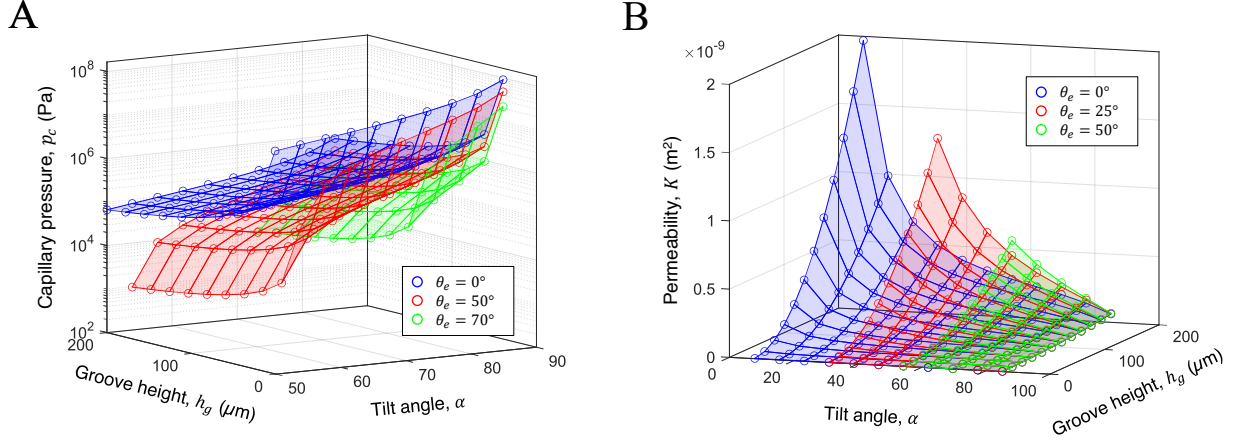
A



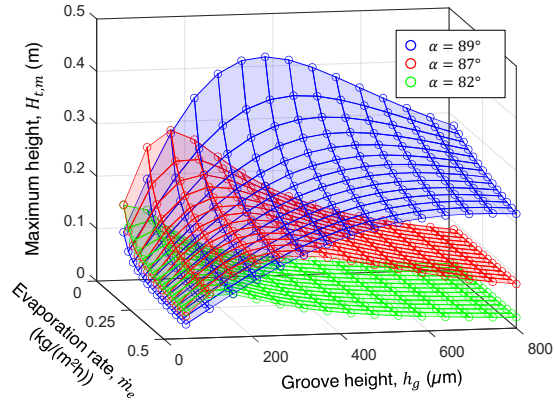
B



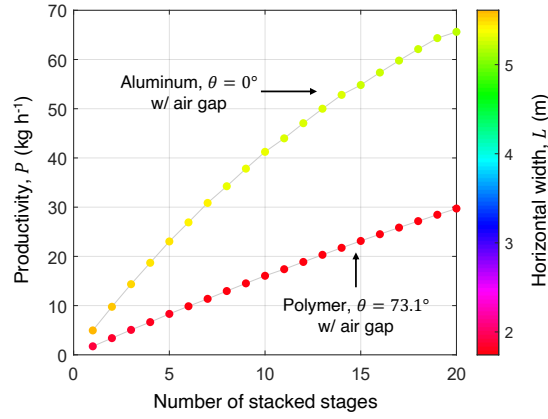
Supplementary Figure S3: **EDS spectroscopy of the laser-etched aluminum after the evaporation test.** (A-B) SEM and EDS spectroscopy images of the proposed capillary material after long-term exposure to micro-filtered water and 1000 W/m². The analyses show a high percentage of contaminants accumulated on the groove walls during the test. Note that the untreated areas (spectra 2 and 4) have low concentrations of contaminants. Elements not shown in the legend were present in a non-significant amount.



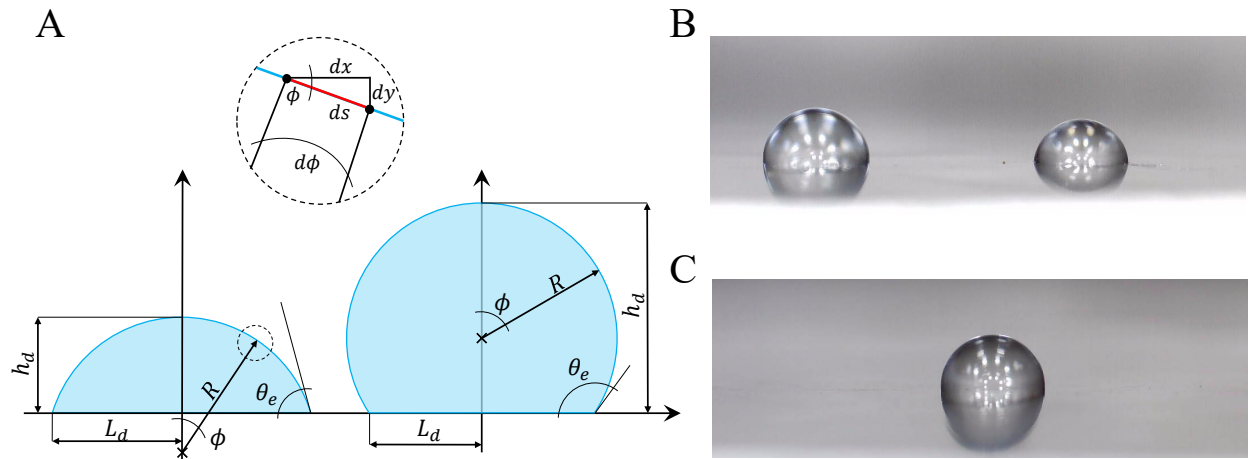
Supplementary Figure S4: **Theoretical modelling of the capillary properties.** Theoretical predictions of (A) the capillary pressure and (B) the absolute permeability for different values of groove height h_g , tilt angle α and contact angle θ_e . The modelling predictions were performed considering an ideally smooth V-shaped groove (see Methods).



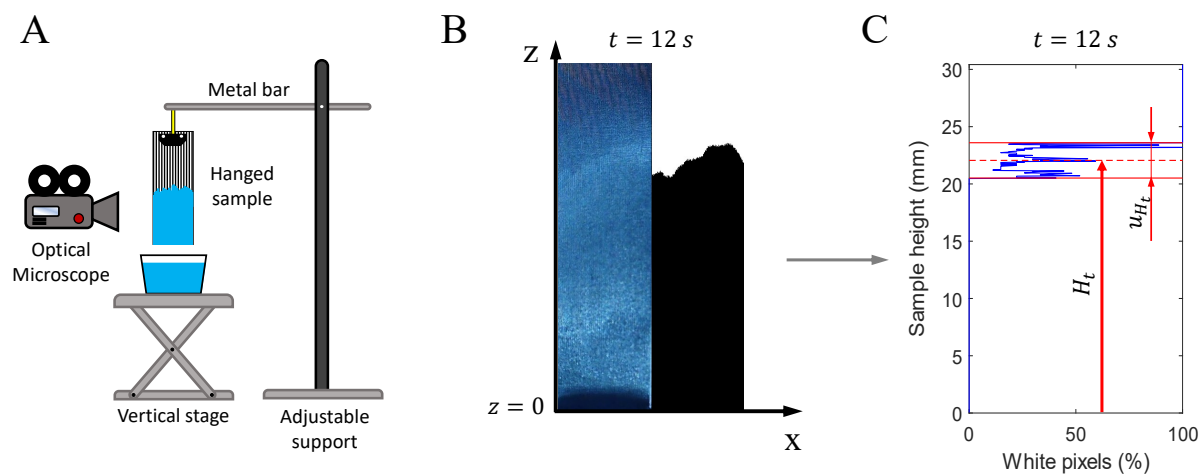
Supplementary Figure S5: **Theoretical Prediction of the wicking performance with different evaporation rates.** Maximum height reached by the water front in vertical wicking test $H_{t,m}$ evaluated for different evaporation rates \dot{m}_e and geometrical grooves parameters, namely height h_g and tilt angle α . The predictions were performed by a novel model employing an explicit time discretization scheme to include the effect of evaporation rate in the wicking transient (see Supplementary Note S6). The results show how the working conditions should be included in the optimization of the geometry, as different \dot{m}_e result in different optimal values of h_g . Furthermore, the predictions show how small variation of α may result in a dramatic decrease of the resulting capillary properties.



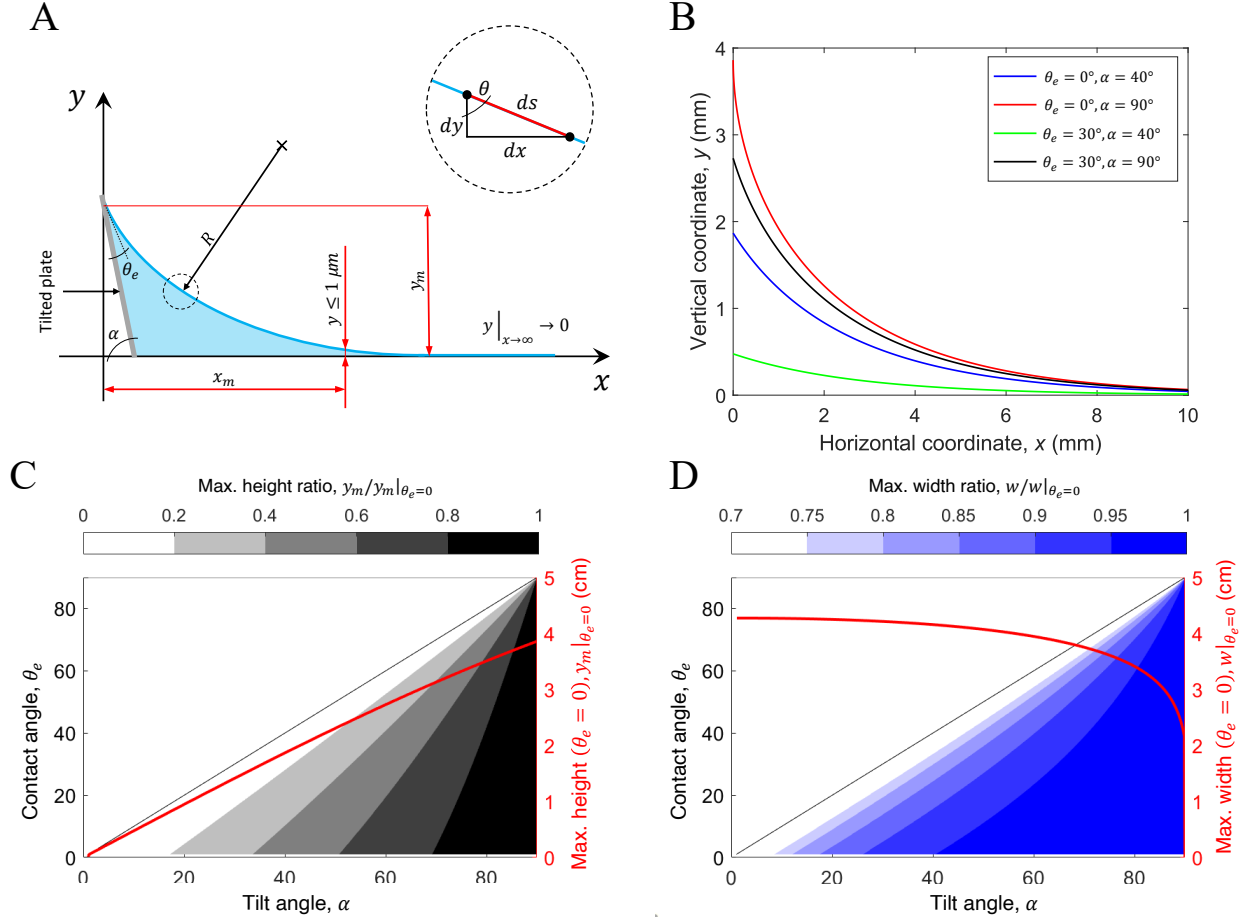
Supplementary Figure S6: **Extrapolation of the performance of the desalination device.** Modeling predictions of the device productivity P achievable by employing two different materials as substrates in both evaporators and condensers: nylon, with $\theta_e = 73.1^\circ$; an ideally wettable aluminum sheet. Both materials were supposed as provided with optimal grooves, which shape was evaluated via the presented capillary model. The simulations were performed considering a membrane-less configuration. The color bar reports the maximum horizontal width achievable.



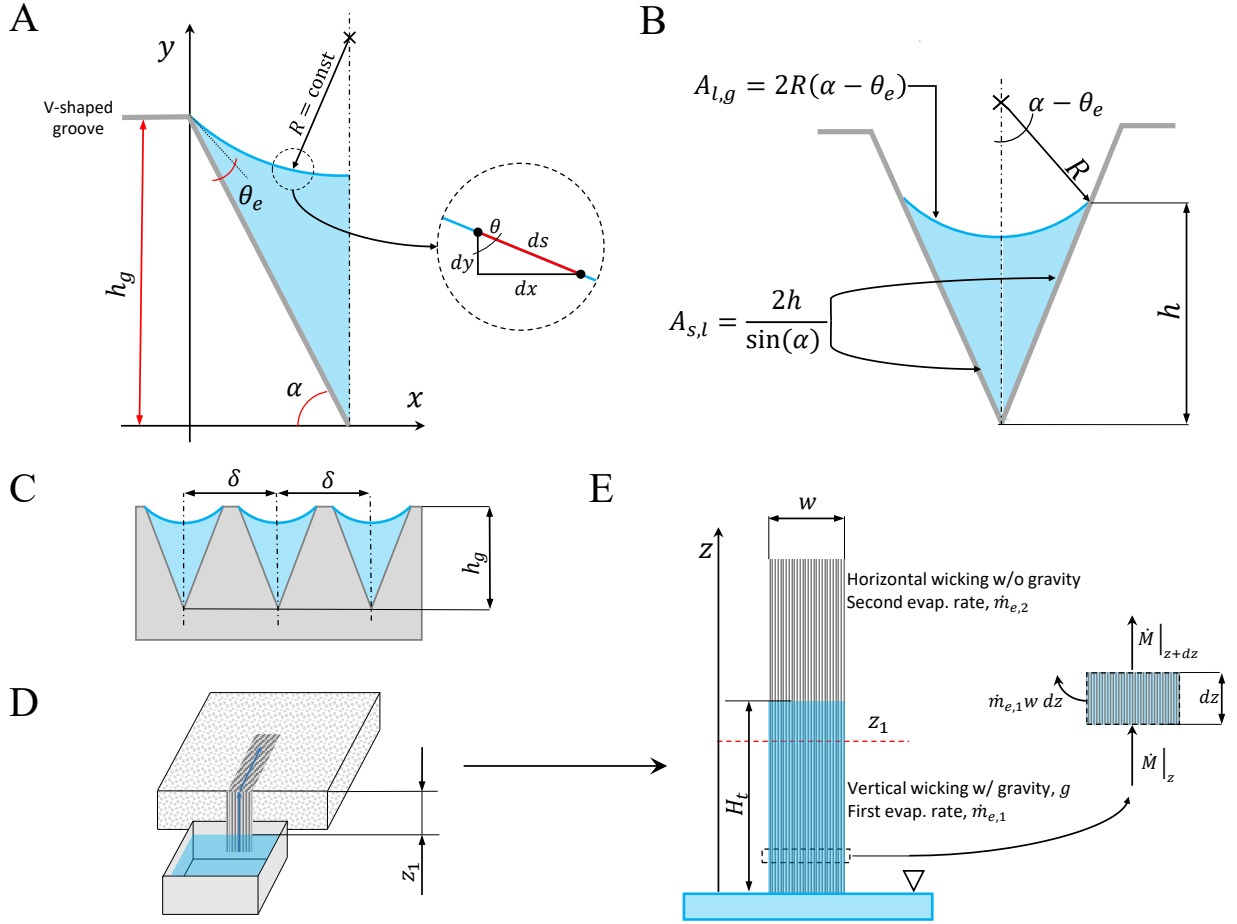
Supplementary Figure S7: **Experimental evaluation of the water-aluminium contact angle.** (A) Schematics of two water droplets under the assumption of negligible effect of gravity on a hydrophilic (left) and hydrophobic (right) surface. (B-C) Millimetre-sized water droplets on a pristine aluminium plate. As it can be observed, the assumption of approximately spherical shape holds both for contact angles lower (B) and greater (C) than $\pi/2$.



Supplementary Figure S8: **Experimental investigation of the wicking performance.** (A) Schematics of the experimental setup and procedure used to perform the vertical wicking experiments. An optical microscope was used to record the vertical wicking experiment of a laser-etched sample hung from an adjustable support. (B-C) The images extracted from the video were post-processed and converted to black/white images via the *imbinarize* routine (B) and were used to estimate the position of the water front (C) by evaluating the percentage of white pixels in the x-axis direction.



Supplementary Figure S9: **Modelling the effects of gravity on the shape of the meniscus.** (A) Schematics of the shape of a meniscus facing an attractive plate tilted by an angle α . The system was supposed to have reached the equilibrium after the plate was immersed in a large reservoir. The red quotes highlight the important quantities for the model: the maximum height reached by the meniscus y_m and the maximum extension of the meniscus from the wall x_m , arbitrarily located where the meniscus height is smaller than $1 \mu\text{m}$. (B) Effects of the equilibrium contact angle θ_e and the plate tilt angle α on the meniscus shape. Lower values of θ_e and higher values of α result in higher capillary rises. (C) Map showing the maximum capillary rise y_m on a tilted flat plate as a function of the tilt angle α and θ_e . The values reported in grey-scale were referred to the maximum capillary rise obtained for $\theta_e = 0$, namely $y_m|_{\theta_e=0}$ (solid red line, referring to the right-hand side vertical axis). (D) Map showing the maximum width of the V-shaped groove $w = 2x_m$ as a function of the tilt angle α and θ_e . The values reported in blue-scale were referred to the maximum capillary rise obtained for $\theta_e = 0$, namely $w|_{\theta_e=0}$ (solid red line, referring to the right-hand side vertical axis). The solid black lines in panels (C) and (D) represent the theoretical limit of the model $\theta_e = \alpha$, which relates to a flat meniscus and, thus, no capillary pressure.



Supplementary Figure S10: **Schematics of the capillary model.** (A-B) Schematics of a sub-millimetre V-shaped groove filled by water highlighting the main parameters in the proposed theoretical model: the groove tilt angle α , the water-groove equilibrium contact angle θ_e and the height of the groove h_g (see section Supplementary Note S1). The model neglects the effect of gravity and the pinning of the meniscus at the edges of the groove. (C) Cross section of the laser-etched aluminium plate highlighting the main geometrical features used to compute the flow parameters of an equivalent porous medium (see section Supplementary Note S4). (D-E) Schematics of the vertical-horizontal imbibition setup including two different evaporation rates. The setup mimics the typical layout of multistage passive desalination devices, where vertical sections (usually exposed to the ambient or partially insulated) feed sea water to the horizontal stack by capillarity. For the sake of simplicity the horizontal stack in panel (D), usually composed by evaporators, condensers, membranes and a solar absorber, was represented as composed by the horizontal laser-etched aluminium sheet only. The model developed neglects the effect of the bend at z_1 on the capillary action.